

# Flat-lens focusing of electrons on the surface of a topological insulator

F. Hassler, A. R. Akhmerov, and C. W. J. Beenakker

*Instituut-Lorentz, Universiteit Leiden, P.O. Box 9506, 2300 RA Leiden, The Netherlands*

(Dated: May, 2010)

We propose the implementation of an electronic Veselago lens on the conducting surface of a three-dimensional topological insulator (such as  $\text{Bi}_2\text{Te}_3$ ). The negative refraction needed for such a flat lens results from the sign change of the curvature of the Fermi surface, changing from a circular to a snowflake-like shape across a sufficiently large electrostatic potential step. No interband transition (as in graphene) is needed. For this reason, and because the topological insulator provides protection against backscattering, the potential step is able to focus a broad range of incident angles. We calculate the quantum interference pattern produced by a point source, generalizing the analogous optical calculation to include the effect of a noncircular Fermi surface (having a nonzero conic constant).

PACS numbers: 73.20.-r, 41.85.Ne, 73.23.Ad, 73.90.+f

## I. INTRODUCTION

Ballistic electron optics relies on the analogy between the Schrödinger equation for electrons and the Helmholtz equation for classical waves to construct devices that can image the flow of electrons in high-mobility semiconductors.<sup>1-4</sup> A variation in electrostatic potential is analogous to a variation in dielectric constant, so that a curved gate electrode can have the refractive power of a lens — as has been demonstrated in the two-dimensional electron gas of a GaAs heterostructure.<sup>5,6</sup> The focal length of this electrostatic lens depends on its curvature, diverging for a flat electrode.

Focusing of light by a flat lens is possible in media with a negative index of refraction. This so-called Veselago lens<sup>7,8</sup> has a focal length proportional to the distance between lens and source, rather than fixed by the lens itself. It is also not limited by the single optical axis of a curved lens and can have a much wider aperture. Photonic crystals can provide the negative refraction needed for a flat lens,<sup>9</sup> as demonstrated experimentally.<sup>10,11</sup>

The electronic analog of a Veselago lens was proposed in the context of graphene,<sup>12</sup> based on the negative refraction of an electron crossing from the conduction band into the valence band. Such interband crossing requires a  $p$ - $n$  junction, which is highly resistive if the interface extends over more than an electron wave length.<sup>13,14</sup> It would be desirable to have a method for producing a flat lens entirely within the conduction band, in order to avoid a resistive interface. It is the purpose of this work to propose such a method, in the context of topological insulators.

Topological insulators have a conducting surface with a Dirac cone of massless, helical low-energy excitations, reminiscent of graphene.<sup>15,16</sup> Indeed, scanning tunneling microscopy has shown that backscattering of the surface electrons is inhibited, as expected from conservation of helicity.<sup>17,18</sup> While the large band gap topological insulator  $\text{Bi}_2\text{Se}_3$  has a nearly circular Dirac cone, in the smaller band gap material  $\text{Bi}_2\text{Te}_3$  the cone is warped in an hexagonal snowflake-like shape.<sup>19-23</sup> The hexagonal warping

of the Fermi surface enhances the quantum interference (Friedel) oscillations in the density of states near an impurity or potential step,<sup>24-27</sup> which for a circular Fermi surface would be suppressed by conservation of helicity.<sup>28</sup>

The electron focusing considered here is an altogether different, semiclassical consequence of the hexagonal warping. The flat lens is formed by a potential step on the surface of the topological insulator, sufficiently high to change the curvature of the Fermi surface from convex to concave. The sign change of the curvature leads to negative refraction and focusing, qualitatively similar to the optical Veselago lens — but quantitatively different because of the nonuniformity of the curvature (quantified by a nonzero conic constant).

In the following two sections, we derive the negative refraction and the line of focal points (caustics), as well as the diffraction pattern produced by a point source. We calculate the curvature and conic constant for the specific case of  $\text{Bi}_2\text{Te}_3$ . We conclude in Sec. IV by comparing with the flat lens formed by a  $p$ - $n$  junction in graphene<sup>12</sup> and by discussing possible experimental realizations in topological insulators.

## II. NEGATIVE REFRACTION AT A POTENTIAL STEP

### A. Negative refraction

Consider an electron propagating approximately along the  $x$ -axis (the optical axis) and impinging at  $x = 0$  onto an electrostatic potential step  $\delta U$  produced by a gate electrode (see Fig. 1). For simplicity, we assume that the optical axis is parallel to an axis of crystallographic symmetry, such that the equi-energy contours are  $\pm k_y$  symmetric. (For the more general case, see App. A.) At constant Fermi energy, the kinetic energy changes from  $E_i$  in the incident (left) region to  $E_t = E_i + \delta U$  in the transmitted (right) region. The equi-energy contour at the left is given locally by  $\delta k_{i,x} = -\frac{1}{2}c_i k_{i,y}^2$ , for a two-dimensional wave vector  $\mathbf{k}_i = (k_{i,0} + \delta k_{i,x}, k_{i,y})$  approximately along

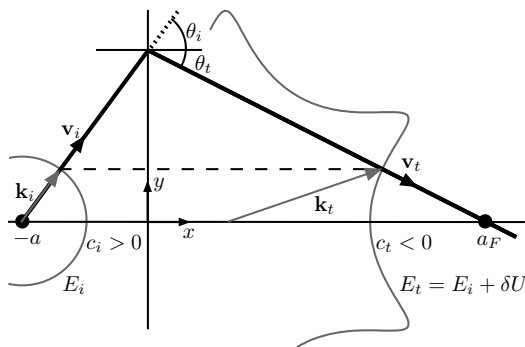


FIG. 1: Negative refraction at a potential step (height  $\delta U$ ) where the curvature of the equi-energy contours (thin curves) changes sign from  $c_i > 0$  to  $c_t < 0$ . An electron (thick arrow) with kinetic energy  $E_i$  is incident at angle  $\theta_i$  and transmitted at angle  $\theta_t$ . Because the curvature changes sign, the electron is negatively refracted with  $\theta_t < 0$  for  $\theta_i > 0$ .

the optical axis, and similarly  $\delta k_{t,x} = -\frac{1}{2}c_t k_{t,y}^2$  at the right. The coefficients  $c_i$  and  $c_t$  are the curvatures of the Fermi surface for normal incidence, at the two sides of the potential step.

The velocity  $\mathbf{v} = \hbar^{-1}\partial E/\partial \mathbf{k}$  is normal to the equi-energy contours, so that the velocities  $\mathbf{v}_i$  and  $\mathbf{v}_t$  in the left and right regions make, respectively, an angle  $\theta_i = c_i k_{i,y}$  and  $\theta_t = c_t k_{t,y}$  with the  $x$ -axis. Conservation of transverse momentum ( $k_{i,y} = k_{t,y}$ ) leads to the linearized Snell's law

$$\theta_t = (c_t/c_i)\theta_i, \quad \text{for } \theta_i, \theta_t \ll 1. \quad (2.1)$$

The inverse curvature plays the role of the refractive index in optics. Negative refraction (meaning  $\theta_i\theta_t < 0$ ) takes place when  $c_i$  and  $c_t$  have opposite signs, as illustrated in Fig. 1.

### B. Noncircular Snell's law

As we will see in the next section, to calculate the image of a point source we will need to include the first nonlinear correction to Eq. (2.1). In optics, where one has a circular equi-energy contour, Snell's law  $c_i \sin \theta_i = c_t \sin \theta_t$  implies the series expansion

$$\theta_t = n_1\theta_i + n_3\theta_i^3 + \mathcal{O}(\theta_i^5), \quad (2.2)$$

with  $n_1 = c_t/c_i$  and  $n_3 = \frac{1}{6}n_1(n_1^2 - 1)$ . More generally, we can write

$$n_1 = c_t/c_i, \quad n_3 = \frac{1}{6}n_1(n_1^2 - 1) + \Delta, \quad (2.3)$$

where  $\Delta$  quantifies the deviation from the optical Snell's law.<sup>31</sup>

The parameter  $\Delta$  vanishes for a circular Fermi surface as in graphene,<sup>12,29,30</sup> but is nonzero for the warped Fermi surfaces of topological insulators. In order to relate  $\Delta$  to the Fermi surface, we parameterize the equi-energy

contour using polar coordinates by  $\mathbf{k} = \kappa(\phi)(\cos \phi, \sin \phi)$ , where  $\phi$  is the angle between the wave vector  $\mathbf{k}$  and the  $x$ -axis and  $\kappa = |\mathbf{k}|$ . A subscript  $i$  or  $t$  distinguishes the parameters at the two sides of the potential step.

The noncircular Snell's law is expressed by the three equations

$$\kappa_t(\phi_t) \sin \phi_t = \kappa_i(\phi_i) \sin \phi_i, \quad (2.4)$$

$$\tan \theta_i = \frac{\kappa_i(\phi_i) \tan \phi_i - \kappa_i'(\phi_i)}{\kappa_i(\phi_i) + \kappa_i'(\phi_i) \tan \phi_i}, \quad (2.5)$$

$$\tan \theta_t = \frac{\kappa_t(\phi_t) \tan \phi_t - \kappa_t'(\phi_t)}{\kappa_t(\phi_t) + \kappa_t'(\phi_t) \tan \phi_t}, \quad (2.6)$$

where  $\kappa' = d\kappa/d\phi$ . The first equation expresses the continuity of the  $y$ -component of the wave vector at the interface  $x = 0$ , while the second and third equations relate the angles  $\theta$  and  $\phi$  of velocity and wave vector (using the fact that  $\mathbf{v}$  is perpendicular to the equi-energy contour). The circular Snell's law  $\kappa_t \sin \theta_t = \kappa_i \sin \theta_i$  is recovered for  $\kappa' = 0$ , when  $\theta = \phi$ .

Near  $\phi = 0$ , the equi-energy contour can be parameterized in terms of the curvature  $c$  and conic constant  $\mathcal{K}$ ,

$$k_y^2 = -(2/c)\delta k_x - (1 + \mathcal{K})(\delta k_x)^2, \quad (2.7)$$

with  $\delta k_x = k_x - \kappa(0)$ . The noncircular Snell's law then expands to Eqs. (2.2)–(2.3) with

$$\Delta = \frac{c_t}{2c_i^3}(c_t^2\mathcal{K}_t - c_i^2\mathcal{K}_i). \quad (2.8)$$

### C. Application to $\text{Bi}_2\text{Te}_3$

We apply these general considerations to the topological insulator  $\text{Bi}_2\text{Te}_3$ . On the [111] surface and close to the center of the Brillouin zone (the  $\Gamma$  point) the Hamiltonian can be approximated by<sup>28</sup>

$$H = \hbar v k(\sigma_y \cos \phi - \sigma_x \sin \phi + \lambda^2 k^2 \sigma_z \cos 3\phi). \quad (2.9)$$

The dispersion relation in the conduction band ( $E > 0$ ) is

$$\begin{aligned} E(\mathbf{k}) &= \hbar v \sqrt{k^2 + (\lambda^2 k^3 \cos 3\phi)^2} \\ &= \hbar v \sqrt{k^2 + \lambda^4 (k_x^3 - 3k_x k_y^2)^2}. \end{aligned} \quad (2.10)$$

The  $\sigma_i$ 's are Pauli matrices acting on the electron spin and  $\phi$  denotes the angle of the wave vector  $\mathbf{k}$  with respect to the  $\Gamma\text{K}$  direction in the Brillouin zone (oriented along the  $x$ -axis). The parameters  $v \approx 4 \cdot 10^5$  m/s and  $\lambda \approx 1$  nm were estimated by fitting to data from angularly resolved spectroscopy.<sup>21,22</sup> (Additional terms quadratic in momentum can be included in the fit, but these do not qualitatively change the dispersion.)

The curvature  $c(E)$  of the equi-energy contour in the  $\Gamma\text{K}$  direction is given by

$$c(E) = \lambda \frac{1 - 6\mathcal{K}^4}{\mathcal{K} + 3\mathcal{K}^5}, \quad (2.11)$$

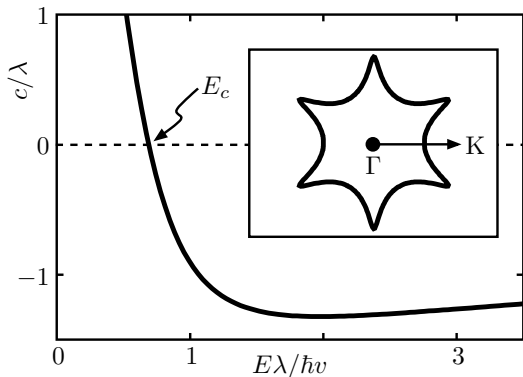


FIG. 2: Curvature  $c(E)$  of the equi-energy contour in the  $\Gamma K$  direction, calculated from Eq. (2.11). The shape changes from convex to concave at energy  $E_c$ . The maximally negative curvature is  $c \approx -1.3$  for  $E \approx 2 \hbar v/\lambda$ , where the equi-energy contour has the snowflake-like shape shown in the inset.

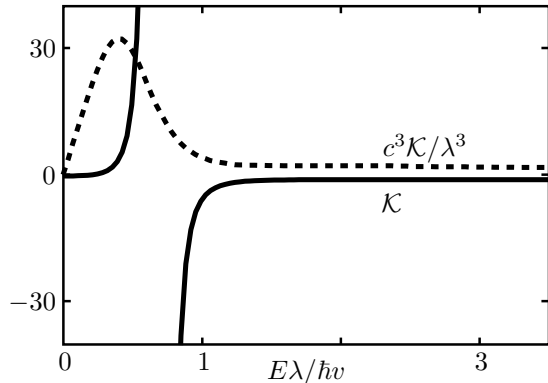


FIG. 3: Plot of the conic constant  $\mathcal{K}$  (solid line) as well as the combination  $c^3\mathcal{K}/\lambda^3$  [appearing in the noncircular Snell's law (2.8)] (dashed line), both as a function of the energy  $E$ . The divergence of  $\mathcal{K}$  is at the energy  $E_c$  where the curvature vanishes.

with  $\varkappa^2 = \xi_+^{1/3} - \xi_-^{1/3}$  defined in terms of

$$\xi_{\pm} = \frac{1}{6\hbar^2 v^2} \left( \sqrt{\frac{4}{3}\hbar^4 v^4 + 9\lambda^4 E^4} \pm 3\lambda^2 E^2 \right). \quad (2.12)$$

The quantity  $\varkappa/\lambda = \kappa(0)$  equals  $|\mathbf{k}|$  at  $\phi = 0$ .

The energy dependence of the curvature is plotted in Fig. 2. As discovered by Fu,<sup>28</sup> the curvature changes sign when  $\varkappa_c^4 = 1/6$ , which corresponds to an energy  $E_c = 6^{-3/4}\sqrt{7}\hbar v/\lambda \approx 0.2\text{eV}$  and a wave vector  $k_c = \varkappa_c/\lambda \approx 0.6\text{nm}^{-1}$ . At the same point the conic constant

$$\mathcal{K}(E) = \frac{3\varkappa^4(35 - 60\varkappa^4 + 72\varkappa^8)}{(1 - 6\varkappa^4)^3} \quad (2.13)$$

diverges and thereby changes sign, cf. Fig. 3.

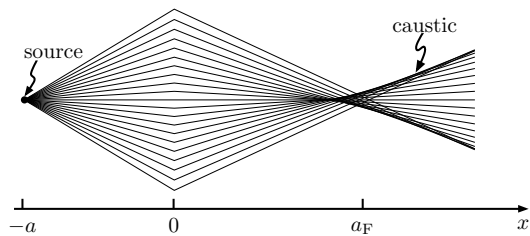


FIG. 4: Classical trajectories refracted at a potential step at  $x = 0$ , with the cusp caustic indicated.

### III. CAUSTICS FROM A POINT SOURCE

#### A. Focusing of classical trajectories

Because of the negative refraction, diverging trajectories become converging at the potential step and then cross at a focal point (see Fig. 4). If a point source is placed at  $(-a, 0)$ , a distance  $a$  from the interface at  $x = 0$ , then the trajectory for an electron incident at an angle  $\theta_i$  and transmitted at an angle  $\theta_t$  is parameterized by

$$y(x; \theta_i) = \begin{cases} (a+x)\tan\theta_i, & \text{for } x < 0, \\ a\tan\theta_i + x\tan\theta_t, & \text{for } x > 0. \end{cases} \quad (3.1)$$

On the optical axis  $y, \theta_i, \theta_t \rightarrow 0$  we obtain the focal point  $(a_F, 0)$ , with

$$a_F = -a/n_1 = -\frac{c_i}{c_t}a, \quad (3.2)$$

proportional to the ratio of the two curvatures. As in the optical Veselago lens,<sup>32,33</sup> the focal point is displaced from the optical axis as we increase the angle of incidence, so that the point  $(a_F, 0)$  is the cusp on a curve of focal points. This caustic curve (called an *astroid*<sup>34</sup>) is visible in Fig. 4 as the envelope of the refracted trajectories.

The caustic curve near  $(a_F, 0)$  is obtained from Eq. (3.1) and the nonlinear Snell's law (2.2) by demanding that  $\partial y/\partial\theta_i = 0$ . We find

$$\alpha(y/a)^2 = (x/a_F - 1)^3, \quad (3.3)$$

with the opening rate of the cusp governed by the parameter

$$\alpha = \frac{27}{8} [1 - (c_t/c_i)^2 - 2(c_i/c_t)\Delta]. \quad (3.4)$$

For  $\Delta = 0$ , so for a circular Fermi surface, this agrees with Refs. 12,33. Depending on the sign of  $\alpha$ , the cusp points away from the potential step (for  $\alpha > 0$ ) or towards the potential step (for  $\alpha < 0$ ). For  $\alpha = 0$  higher than third-order terms in the expansion (2.2) have to be included in order to obtain the caustic curve.

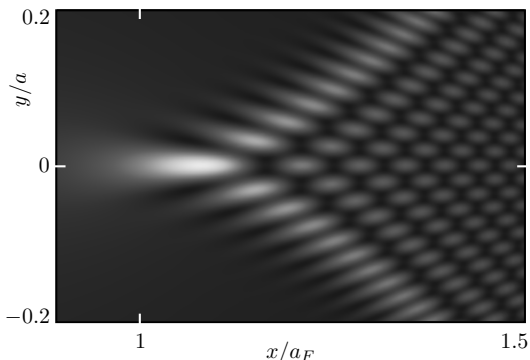


FIG. 5: Gray-scale plot of the current density  $j(\mathbf{r})$  as a function of position  $\mathbf{r} = (x, y)$  near the focal point  $(a_F, 0)$  for a source located at  $(-a, 0)$ , calculated from Eqs. (3.7) and (3.8) for  $\alpha = 1$  and  $a/c_i = 100$ . Lighter shades of gray indicate higher current densities. The cusp caustic starting at the focal point is decorated by oscillations on the scale of the wavelength.

### B. Quantum interference near the focal point

The diffraction pattern near a cusp caustic has a universal functional form (Pearcey integral),<sup>35,36</sup> but the parameters governing that function are modified for non-circular equi-energy contours. We calculate the wave function  $\Psi$  at a point  $\mathbf{r} = (x, y)$  near the cusp by summing over partial waves  $\Psi_{y_0}$  from points  $\mathbf{r}_0 = (0, y_0)$  along the potential step [excited by a point source at  $\mathbf{r}_{\text{source}} = (-a, 0)$ ]. In the far-field approximation, for  $a$  and  $a_F$  large compared to the wave length, the partial waves have the simple form

$$\Psi_{y_0} = \begin{pmatrix} u_{y_0} \\ v_{y_0} \end{pmatrix} A_{y_0} e^{i\Phi_{y_0}}, \quad (3.5)$$

$$\Phi_{y_0} = \mathbf{k}_i \cdot (\mathbf{r}_0 - \mathbf{r}_{\text{source}}) + \mathbf{k}_t \cdot (\mathbf{r} - \mathbf{r}_0). \quad (3.6)$$

The amplitude  $A_{y_0}$  and spinor components  $u_{y_0}, v_{y_0}$  vary slowly as  $y_0$  is varied on the scale of the wave length, so we fix their values at  $A_0, u_0, v_0$  and retain only the  $y_0$  dependence of the phase  $\Phi_{y_0}$ .

In the optical case, the wave vectors  $\mathbf{k}_i$  and  $\mathbf{k}_t$  at the two sides of the interface point in the direction of the velocity and hence are parallel to the rays  $\mathbf{r}_0 - \mathbf{r}_{\text{source}}$  and  $\mathbf{r} - \mathbf{r}_0$ . For a noncircular Fermi surface this is no longer true and we have to take into account the difference between the angles  $\phi_i, \phi_t$  and  $\theta_i = \arctan(y_0/a)$  and  $\theta_t = \arctan[(y - y_0)/x]$  which the wave vectors and the rays make with the  $x$ -axis. The relation between  $\phi$  and  $\theta$  is expressed by Eqs. (2.5) and (2.6), in terms of the radial parameter  $\kappa(\phi) = |\mathbf{k}|$  of the equi-energy contour.

We expand  $\Phi_{y_0}$  in a power series in  $y_0$ . Near the cusp caustic (3.3),  $y/a = \mathcal{O}(y_0/a)^3$  while  $x/a_F - 1 =$

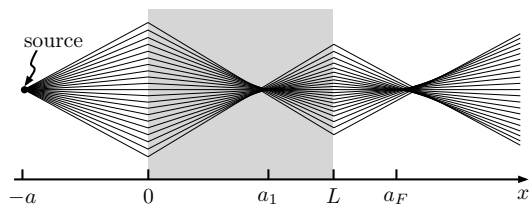


FIG. 6: Flat lens, with two potential steps (upward at  $x = 0$  and downward at  $x = L$ ) and two cusp caustics (at  $x = a_1$  and  $x = a_F$ ).

$\mathcal{O}(y_0/a_F)^2$ . To fourth order in  $y_0$  we find

$$\Phi_{y_0} = \kappa_i(0)a + \kappa_t(0)x - \frac{yy_0}{c_t a_F} - \frac{(x - a_F)y_0^2}{2c_t a_F^2} + \frac{\alpha y_0^4}{27c_t a_F a^2}, \quad (3.7)$$

with  $\alpha$  given by Eq. (3.4). One readily checks that the stationary phase equations  $\partial\Phi_{y_0}/\partial y_0 = 0 = \partial^2\Phi_{y_0}/\partial y_0^2$  give the caustic curve (3.3). (These equations correspond to the geometric optics limit  $c_t \rightarrow 0$  of vanishing wavelength.)

The current density  $j(\mathbf{r})$  follows upon integration over  $y_0$ ,

$$j(\mathbf{r}) = j_0 \left| \int_{-\infty}^{\infty} dy_0 e^{i\Phi_{y_0}} \right|^2, \quad (3.8)$$

with  $j_0$  a constant proportional to the product of the injection rate at the source and the transmission probability  $T$  through the potential step. By rescaling the integration variable  $y_0 \rightarrow ay'_0$ , we see that the current density (3.8) as a function of  $x/a_F$  and  $y/a$  depends only on the two parameters  $\alpha$  and  $a/c_i$ . Figure 5 is a plot of this current density, showing the characteristic interference pattern of a cusp caustic.

### C. Focusing by a flat lens

The flat lens in Fig. 6 is formed by the potential profile  $U(x) = \delta U$  for  $0 < x < L$ ,  $U(x) = 0$  otherwise. We denote the Fermi surface curvatures (of opposite sign) inside the lens ( $0 < x < L$ ) by  $c_{\text{lens}}$  and outside ( $x < 0$ ,  $x > L$ ) by  $c_0$ . Negative refraction at the two potential steps at  $x = 0$  and  $x = L$  focuses a source at  $x = -a$  on the optical axis ( $y = 0$ ) first onto the point  $a_1 = -(c_0/c_{\text{lens}})a$  inside the lens and then onto the point

$$a_F = (1 - c_{\text{lens}}/c_0)L - a \quad (3.9)$$

outside the lens (provided it is sufficiently thick,  $|c_{\text{lens}}L| > |c_0a|$ ).

The classical trajectories are now parameterized by

$$y(x; \theta_i) = \begin{cases} (a+x)\tan\theta_i, & \text{for } x < 0, \\ a\tan\theta_i + x\tan\theta_t, & \text{for } 0 < x < L, \\ (a+x-L)\tan\theta_i + L\tan\theta_t, & \text{for } x > L. \end{cases} \quad (3.10)$$

The relation between  $\theta_t$  and  $\theta_i$  is still given by Eq. (2.2), with

$$n_1 = c_{\text{lens}}/c_0, \quad n_3 = \frac{1}{6}n_1(n_1^2 - 1) + \Delta. \quad (3.11)$$

The cusp caustic near  $(a_F, 0)$  has the form

$$\beta(y/a)^2 = (x/a_F - 1)^3, \quad (3.12)$$

as in Eq. (3.3) but with a different parameter

$$\beta = \frac{27}{8} \frac{L a^2}{a_F^3} \frac{c_{\text{lens}}}{c_0} [1 - (c_{\text{lens}}/c_0)^2 - 2(c_0/c_{\text{lens}})\Delta]. \quad (3.13)$$

Notice that  $\alpha$  and  $\beta$  have the opposite sign (because of the factor  $c_{\text{lens}}/c_0 < 0$ ), so that the cusps inside and outside the lens point in opposite directions (as visible in Fig. 6).

The flat-lens diffraction pattern near the caustic is given by the same Pearcey integral (3.7)–(3.8) as for a single interface, but with different coefficients,

$$j(\mathbf{r}) = j_0 \left| \int_{-\infty}^{\infty} dy_0 \exp \left[ -\frac{yy_0}{c_0 a_F} - \frac{(x - a_F)y_0^2}{2c_0 a_F^2} + \frac{\beta y_0^4}{27 c_0 a_F a^2} \right] \right|^2. \quad (3.14)$$

Thus, the interference pattern that can be observed near  $a_F$  looks similar to Fig. 5.

## IV. DISCUSSION

### A. Intraband versus interband negative refraction

The Veselago lens at a  $p$ - $n$  junction in graphene<sup>12</sup> uses *interband* scattering to achieve negative refraction. In contrast, the mechanism considered here is *intraband*, operating entirely within the conduction band. The  $p$ - $n$  junction has one special feature which our setup lacks, which is the possibility to use electron-hole symmetry to collapse the caustic curve onto a single focal point (when  $c_t = -c_i$ ). In our setup the Fermi surfaces at the two sides of the potential step are not related by any symmetry relation, so in general the two Fermi surface curvatures  $c_t$  and  $c_i$  will be different in magnitude.

The main advantage of an intraband over an interband mechanism for negative refraction is that the transmission probability  $T$  can be much higher. Typically, the width  $d$  of the potential step will be large compared to the Fermi wave length  $\lambda_F = 2\pi/k_F$ . Intraband transmission is then realized with unit probability, up to exponentially small backscattering corrections:  $T = 1 - \mathcal{O}(e^{-k_F d})$ . Interband transmission, in contrast, has  $T \simeq \exp(-k_F d \sin^2 \theta_i)$ , so it is exponentially suppressed for angles further than  $\sqrt{\lambda_F/d}$  from normal incidence.<sup>14</sup>

### B. Experimental realization

Realization of the intraband flat lens proposed here, requires firstly a topological insulator with sufficiently long mean free paths to ensure ballistic motion of the electrons from source to focus. Sufficiently pure single crystals should make this possible.

Secondly, and more specifically, the curvature of the Fermi surface should be tunable from positive to negative values by a gate voltage. From spectroscopic data<sup>22</sup> for Sn-doped Bi<sub>2</sub>Te<sub>3</sub> we would estimate that a potential step  $\delta U \simeq -0.1$  eV would produce a positive curvature inside a narrow strip and a negative curvature outside (as in Fig. 6). The strip itself would also allow for bulk conduction, because in Bi<sub>2</sub>Te<sub>3</sub> a positively curved Dirac cone of surface states overlaps with bulk states. Since the regions outside the lens have only surface conduction, we do not expect the bulk states inside the lens to spoil the focusing.

A point source can be created, for example, using the “needle-anvil” technique developed for point contact spectroscopy,<sup>37</sup> or alternatively using a scanning tunneling microscope (STM). For the spatially resolved detection of the current density distribution an STM tip is most convenient. Such a setup would provide a sensitive probe of the nonspherical Fermi surface of a topological insulator, in a similar way as has recently been proposed for metals.<sup>38</sup>

### Acknowledgments

We acknowledge fruitful discussions with M. Wimmer. This research was supported by the Dutch Science Foundation NWO/FOM and by an ERC Advanced Investigator grant.

### Appendix A: Sheared caustic curve for tilted potential step

In the main text we have assumed for simplicity that the potential step is perpendicular to the  $\Gamma K$  direction in Fig. 2. Then only odd powers of  $\theta_i$  appear in the expansion (2.2). If the potential step is tilted relative to this crystallographic axis, then the cusp caustic persists but in a distorted form, as we now derive.

Including also even powers of  $\theta_i$  in Eq. (2.2) one would have the expansion

$$\theta_t = n'_0 + n'_1 \theta_i + n'_2 \theta_i^2 + n'_3 \theta_i^3 + \mathcal{O}(\theta_i^4). \quad (A1)$$

By rotating the coordinate axis, we can set  $n'_0 = 0$ . The expressions simplify if we expand in powers of  $\tan \theta_i$ ,

$$\tan \theta_t = m_1 \tan \theta_i + m_2 \tan^2 \theta_i + m_3 \tan^3 \theta_i + \mathcal{O}(\tan^4 \theta_i). \quad (A2)$$

From Eq. (3.1), demanding  $\partial y/\partial\theta_i = 0$ , we obtain the implicit caustic equation

$$\begin{pmatrix} x \\ y \end{pmatrix} = a(m_1 + 2m_2 \tan\theta_i + 3m_3 \tan^2\theta_i)^{-1} \\ \times \begin{pmatrix} -1 \\ (m_2 + 2m_3 \tan\theta_i) \tan^2\theta_i \end{pmatrix}. \quad (\text{A3})$$

The cusp of the caustic is given by the condition  $\partial x/\partial\theta_i = 0$ . It is at  $\tan\theta_{i0} = -m_2/3m_3$ . In order to remain in the region of validity of the expansion (A1), we assume that  $|m_2| \ll |m_3|$  so that the tilt remains small. Then the cusp is located at

$$\begin{pmatrix} x_0 \\ y_0 \end{pmatrix} = \begin{pmatrix} -a/m_1 \\ 0 \end{pmatrix}. \quad (\text{A4})$$

We now expand Eq. (A3) near  $\tan\theta_i = \tan\theta_{i0}$  to third order in  $\delta = \tan\theta_i - \tan\theta_{i0}$ ,

$$\begin{pmatrix} x - x_0 \\ y - y_0 \end{pmatrix} = am_3 m_1^{-1} \begin{pmatrix} 3m_1 \delta^2 \\ -m_2 m_3^{-1} \delta^2 + 2\delta^3 \end{pmatrix}. \quad (\text{A5})$$

Eliminating  $\delta$  yields the caustic curve

$$\gamma[y - y_0 + \epsilon(x - x_0)]^2 = (x - x_0)^3, \quad (\text{A6})$$

with coefficients  $\gamma = 27am_3/4m_1^4$  and  $\epsilon = m_1 m_2/3m_3$ . Equation (A6) has the general form of a sheared cusp caustic from catastrophe theory.<sup>39</sup>

- 
- <sup>1</sup> J. Spector, J. S. Weiner, H. L. Störmer, K. W. Baldwin, L. N. Pfeiffer, and K. W. West, *Surf. Sci.* **263**, 240 (1992).
- <sup>2</sup> H. van Houten and C. W. J. Beenakker, in *Confined Electrons and Photons: New Physics and Applications*, ed. by E. Burstein and C. Weisbuch, NATO ASI Series B **340**, 269 (Plenum, New York, 1995).
- <sup>3</sup> B. J. LeRoy, *J. Phys. Cond. Matt.* **15**, R1835 (2003).
- <sup>4</sup> M. A. Topinka, R. M. Westervelt, and E. J. Heller, *Phys. Today* **56** (12), 47 (2003).
- <sup>5</sup> J. Spector, H. L. Störmer, K. W. Baldwin, L. N. Pfeiffer, and K. W. West, *Appl. Phys. Lett.* **56**, 967 (1990).
- <sup>6</sup> U. Sivan, M. Heiblum, C. P. Umbach, and H. Shtrikman, *Phys. Rev. B* **41**, 7937 (1990).
- <sup>7</sup> V. G. Veselago, *Sov. Phys. Usp.* **10**, 509 (1960).
- <sup>8</sup> J. B. Pendry and D. R. Smith, *Phys. Today* **57** (6), 37 (2004).
- <sup>9</sup> M. Notomi, *Phys. Rev. B* **62**, 10696 (2000).
- <sup>10</sup> P. V. Parimi, W. T. Lu, P. Vodo, and S. Sridhar, *Nature* **426**, 404 (2003).
- <sup>11</sup> E. Cubukcu, K. Aydin, E. Ozbay, S. Foteinopoulou, and C. M. Soukoulis, *Nature* **423**, 604 (2003).
- <sup>12</sup> V. V. Cheianov, V. Fal'ko, and B. L. Al'tshuler, *Science* **315**, 1252 (2007).
- <sup>13</sup> M. I. Katsnelson, K. S. Novoselov, and A. K. Geim, *Nature Phys.* **2**, 620 (2006).
- <sup>14</sup> V. V. Cheianov and V. I. Fal'ko, *Phys. Rev. B* **74**, 041403 (2006).
- <sup>15</sup> X.-L. Qi and S.-C. Zhang, *Phys. Today* **63** (1), 33 (2010).
- <sup>16</sup> M. Z. Hasan and C. L. Kane, arXiv:1002.3895.
- <sup>17</sup> P. Roushan, J. Seo, C. V. Parker, Y. S. Hor, D. Hsieh, D. Qian, A. Richardella, M. Z. Hasan, R. J. Cava, and A. Yazdani, *Nature* **460**, 1106 (2009).
- <sup>18</sup> T. Zhang, P. Cheng, X. Chen, J.-F. Jia, X. Ma, K. He, L. Wang, H. Zhang, X. Dai, Z. Fang, X. Xie, and Q.-K. Xue, *Phys. Rev. Lett.* **103**, 266803 (2009).
- <sup>19</sup> H. Zhang, C.-X. Liu, X.-L. Qi, X. Dai, Z. Fang, and S.-C. Zhang, *Nature Phys.* **5**, 438 (2009).
- <sup>20</sup> Y. Xia, D. Qian, D. Hsieh, L. Wray, A. Pal, H. Lin, A. Bansil, D. Grauer, Y. S. Hor, R. J. Cava, and M. Z. Hasan, *Nature Phys.* **5**, 398 (2009).
- <sup>21</sup> D. Hsieh, Y. Xia, D. Qian, L. Wray, J. H. Dil, F. Meier, J. Osterwalder, L. Patthey, J. G. Checkelsky, N. P. Ong, A. V. Fedorov, H. Lin, A. Bansil, D. Grauer, Y. S. Hor, R. J. Cava, and M. Z. Hasan, *Nature* **460**, 1101 (2009).
- <sup>22</sup> Y. L. Chen, J. G. Analytis, J.-H. Chu, Z. K. Liu, S.-K. Mo, X. L. Qi, H. J. Zhang, D. H. Lu, X. Dai, Z. Fang, S. C. Zhang, I. R. Fisher, Z. Hussain, and Z.-X. Shen, *Science* **325**, 178 (2009).
- <sup>23</sup> M. Z. Hasan, H. Lin, and A. Bansil, *Physics* **2**, 108 (2009).
- <sup>24</sup> Z. Alpichshev, J. G. Analytis, J.-H. Chu, I. R. Fisher, Y. L. Chen, Z. X. Shen, A. Fang, and A. Kapitulnik, *Phys. Rev. Lett.* **104**, 016401 (2010).
- <sup>25</sup> X. Zhou, C. Fang, W.-F. Tsai, and J. Hu, *Phys. Rev. B* **80**, 245317 (2009).
- <sup>26</sup> W.-C. Lee, C. Wu, D. P. Arovas, and S.-C. Zhang, *Phys. Rev. B* **80**, 245439 (2009).
- <sup>27</sup> Q.-H. Wang, D. Wang, and F.-C. Zhang, *Phys. Rev. B* **81**, 035104 (2010).
- <sup>28</sup> L. Fu, *Phys. Rev. Lett.* **103**, 266801 (2009).
- <sup>29</sup> J. Cserti, A. Pályi, and Cs. Péterfalvi, *Phys. Rev. Lett.* **99**, 246801 (2007).
- <sup>30</sup> Cs. Péterfalvi, A. Pályi, and J. Cserti, *Phys. Rev. B* **80**, 075416 (2009).
- <sup>31</sup> We assume that the potential step is perpendicular to the GK direction in Fig. 2, so that only odd powers of  $\theta_i$  appear in the expansion (2.2). This assumption is relaxed in App. A.
- <sup>32</sup> A. P. Anyutin, *J. Comm. Techn. Electr.* **53**, 387 (2008).
- <sup>33</sup> M. L. Shendeleva, *J. Microsc.* **229**, 452 (2008).
- <sup>34</sup> E. H. Lockwood, *A Book of Curves* (Cambridge University, Cambridge, 1961).
- <sup>35</sup> T. Pearcey, *Phil. Mag.* **37**, 311 (1946).
- <sup>36</sup> M. V. Berry and C. Upstill, *Prog. Opt.* **18**, 257 (1980).
- <sup>37</sup> Yu. G. Naidyuk and I. K. Yanson, *Point Contact Spectroscopy* (Springer, Berlin, 2005).
- <sup>38</sup> A. Weismann, M. Wenderoth, S. Lounis, P. Zahn, N. Quaaas, R. G. Ulbrich, P. H. Dederichs, and S. Blügel, *Science* **323**, 1190 (2009).
- <sup>39</sup> J. F. Nye and J. H. Hannay, *J. Mod. Optics* **31** 115 (1984).